International Journal of Mass Spectrometry 438 (2019) 124–134

Contents lists available at ScienceDirect

International Journal of Mass Spectrometry

journal homepage: www.elsevier.com/locate/ijms

Full Length Article

Gas-phase structures of protonated arabino nucleosides

L.A. Hamlow[a], C.C. He[a], Zachary J. Devereaux[a], H.A. Roy[a], N.A. Cunningham[a], Erik O. Soley[a], G. Berden[b], J. Oomens[b], M.T. Rodgers[a,*]

[a] Department of Chemistry, Wayne State University, Detroit, MI, 48202, United States
[b] Radboud University, Institute for Molecules and Materials, FELIX Laboratory, Toernooiveld 7c, 6525ED, Nijmegen, the Netherlands

ARTICLE INFO

Article history:
Received 21 November 2018
Received in revised form 4 January 2019
Accepted 7 January 2019
Available online 7 January 2019

Keywords:
Adenine arabinoside
Cytosine arabinoside
Guanine arabinoside
Uracil arabinoside
Infrared multiple photon dissociation action spectroscopy
Electronic structure calculations
Sugar puckering
Nucleobase orientation
Protonation

ABSTRACT

Nucleoside modification plays an important role in the native function of DNA and RNA and is also an important synthetic tool for pharmaceuticals. The gas-phase structures of several protonated arabino nucleosides, an important family of modified nucleoside pharmaceuticals, are examined in this work. Infrared multiple photon dissociation action spectra are collected for the protonated forms of the adenine, cytosine, guanine, and uracil arabinosides ([araAdo+H]$^+$, [araCyd+H]$^+$, [araGuo+H]$^+$, and [araUrd+H]$^+$) in the IR fingerprint and hydrogen-stretching regions. Electronic structure calculations are performed to determine low-energy conformers of [araAdo+H]$^+$, [araCyd+H]$^+$, [araGuo+H]$^+$, and [araUrd+H]$^+$, and generate predicted IR spectra for comparison to experiments. Conformers displaying a unique O2′H···O5′ hydrogen-bonding interaction are populated in each of these systems. Conformers exhibiting hydrogen-bonding interactions between the nucleobase and O5′ are also found to display good agreement with the measured spectra. Competition between sugar–sugar, and nucleobase–sugar hydrogen bonding reveals a preference for [araCyd+H]$^+$, [araGuo+H]$^+$, and [araUrd+H]$^+$ to stabilize the sugar ring pucker over the nucleobase rotation. N3 protonation of [araAdo+H]$^+$ provides a very strong N3H$^+$···O5′ hydrogen-bonding interaction, such that nucleobase–sugar hydrogen-bonding takes energetic preference over stabilization of the sugar puckering. However, conformers exhibiting each mode of hydrogen bonding contribute to the measured spectrum of [araAdo+H]$^+$.

© 2019 Elsevier B.V. All rights reserved.

1. Introduction

Modified nucleoside analogs have played an important pharmacological role in a variety of treatments since the 1960s [1–3]. Nucleosides containing an arabinose sugar (arabino nucleosides or arabinosides, araNuo) instead of a ribose or 2′-deoxyribose sugar, were discovered following the isolation of spongothymidine (thymine arabinoside) and spongouridine (uracil arabinoside, araUrd) from marine sponges in the 1950s [4–6]. Arabinose differs from ribose in the inversion of the stereochemistry at the 2′-position. For a nucleoside this results in the 2′-hydroxyl moiety lying on the same side of the sugar ring as the nucleobase and 5′-hydroxyl moiety. Two important, pharmaceutically active, nucleoside analogs from the 1960s–1970s are cytosine arabinoside (cytarabine, araCyd) [7] and adenine arabinoside (vidarabine, araAdo). Cytarabine found pharmaceutical application in the treatment of a number of leukemias [8,9], where it is still used today, whereas vidarabine found use as an antiviral agent [10]. Both cytarabine [11] and vidarabine [12] retain some degree of transport into the cell and have been found to inhibit DNA synthesis [13,14]. Previously the conformations of arabinosides have been studied by NMR [15,16], crystallography [17,18] and gas-phase calculations [19] in order to understand the conformational states of the arabinosides and how they may differ from those of the canonical nucleosides. In solution the location of the 2′- and 5′-hydroxy substituents on the same side of the sugar ring results in a repulsive interaction between these groups [16], whereas gas-phase calculations and crystal structures indicate that a stabilizing intramolecular hydrogen-bonding interaction between O2′ and O5′ is a prominent feature, with the 2′-hydroxyl preferentially serving as the hydrogen-bond donor [17,19]. Understanding the differences in intrinsic conformational preferences of the arabinosides versus the canonical ribonucleosides and 2′-deoxyribonucleosides may help better elucidate the structural changes their incorporation into DNA may bring.

Abbreviations: araAdo, adenine arabinoside; araCyd, cytosine arabinoside; araGuo, guanine arabinoside; araUrd, uracil arabinoside; IRMPD, infrared multiple photon dissociation; FELIX, free electron laser for infrared experiment.

* Corresponding author at: 5101 Cass Ave, Detroit, MI, 48202, United States.
E-mail address: mrodgers@chem.wayne.edu (M.T. Rodgers).

https://doi.org/10.1016/j.ijms.2019.01.005
1387-3806/© 2019 Elsevier B.V. All rights reserved.

Previous studies into the gas-phase conformations of the protonated canonical RNA and DNA nucleosides by IRMPD action spectroscopy [20–29] have often been unable to clearly differentiate the spectral signatures of different sugar conformations. This is compounded by the largely interchangeable O2′H···O3′ and O3′H···O2′ hydrogen-bonding interactions that stabilize the RNA nucleosides. The unique O2′H···O5′ hydrogen-bonding interaction of the arabino nucleosides should present a different hydrogen-stretching spectral signature than those between the 2′- and 3′-hydroxyl substituents. Different spectral signatures might also arise in the IR fingerprint region due to interactions between the nucleobase and 2′-hydroxyl substituent. Coupled with the additional stabilization offered to C2′-*endo*-like sugar puckerings by the O2′H···O5′ hydrogen-bonding interaction, these different spectral signatures may aid in the differentiation of sugar conformations in the experimental IRMPD spectrum.

2. Experimental and computational description

2.1. Materials

Structures of the four arabinose nucleosides studied in this work are shown in Fig. 1. The araGuo and araAdo nucleosides were purchased from Metkinen Chem (Kuopio, Finland), whereas araUrd and araCyd were purchased from Sigma-Aldrich (St. Louis, MO, USA). HPLC grade methanol, water, and acetic acid used during experiments in the IR fingerprint region for all of the protonated arabinosides, as well as the hydrogen-stretching region for $[araAdo+H]^+$ were purchased from Sigma Aldrich (Zwijndrecht, The Netherlands). The HPLC grade methanol and glacial acetic acid used for experiments in the hydrogen-stretching region of $[araGuo+H]^+$, $[araCyd+H]^+$, and $[araUrd+H]^+$ were purchased from Fischer Scientific (Waltham, MA, USA). The HPLC grade water for these experiments was purchased from Sigma Aldrich (St. Louis, MO, USA).

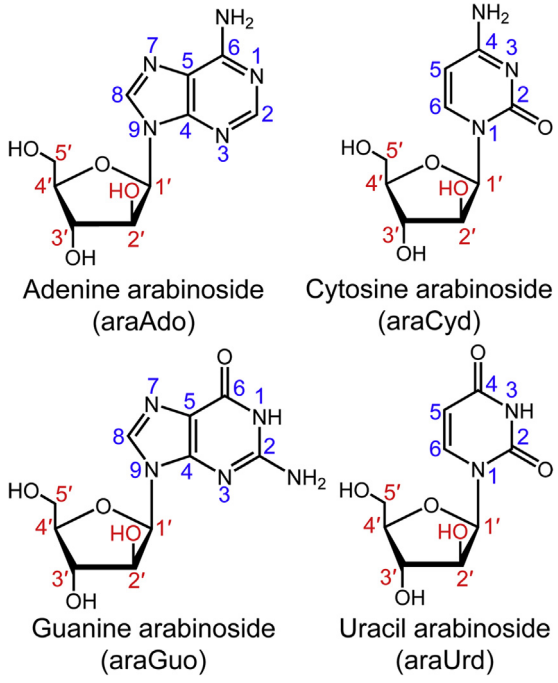

Fig. 1. Structures of neutral adenine arabinoside, cytosine arabinoside, guanine arabinoside, and uracil arabinoside, with atom numbering of the nucleobase and sugar moieties shown.

2.2. Photodissociation

IRMPD action spectra in the IR fingerprint region were measured for $[araAdo+H]^+$, $[araGuo+H]^+$, $[araCyd+H]^+$, and $[araUrd+H]^+$ in a custom-built 4.7 T Fourier transform ion cyclotron resonance mass spectrometer (FT-ICR MS) [30,31]. Protonated ions were generated by electrospray ionization from arabino nucleoside solutions diluted to 1 mM introduced at 7 μL/min to a "Z-Spray" source. Ions were accumulated and thermalized in a hexapole ion guide before being pulsed into the ICR cell through a quadrupole bender and an octopole ion guide. The protonated ions of interest, $[araAdo+H]^+$, $[araCyd+H]^+$, $[araGuo+H]^+$, and $[araUrd+H]^+$, were isolated using stored waveform inverse Fourier transform (SWIFT) techniques. A broadly-tunable free electron laser for infrared experiments (FELIX, repetition rate 10 Hz, bandwidth 0.3% of central frequency, energy up to 70 mJ/pulse) [32] was used to irradiate the trapped ions for 1.6 s, except for $[araCyd+H]^+$, which was irradiated for 2.2 s, in the range of 600–1900 cm^{-1}.

An IRMPD action spectrum in the hydrogen-stretching region (3300–3800 cm^{-1}) was collected for $[araAdo+H]^+$ on the 4.7 T FT-ICR MS described previously, coupled to an optical parametric oscillator/optical parametric amplifier (OPO) laser (LaserVision, Bellevue, WA, repetition rate 10 Hz, bandwidth 3 cm^{-1}, energy 17 mJ/pulse). IRMPD action spectra for $[araCyd+H]^+$, $[araGuo+H]^+$, and $[araUrd+H]^+$ were collected over the same range on a modified Bruker amaZon ETD quadrupole ion trap (QIT-MS), coupled to an OPO laser (LaserVision, Bellevue, WA) described elsewhere [33,34]. Solutions with 25 μM of the relevant arabinoside, acidified with ~1% acetic acid, in 50:50 methanol:water were introduced to the electrospray emitter at 3 μL/min to generate the protonated arabinoside ions. After isolation, $[araCyd+H]^+$, $[araGuo+H]^+$, and $[araUrd+H]^+$ were irradiated for 0.5 s in the QIT MS, whereas $[araAdo+H]^+$ was irradiated for 2.5 s in the FT-ICR MS. IRMPD yields at each frequency were calculated from the measured ion intensities for all experiments as follows.

$$IRMPD\ Yield = \sum_i I_{fragment_i} / (I_{[araNuo+H]^+} + \sum_i I_{fragment_i}) \quad (1)$$

The IRMPD yield in the IR fingerprint region was corrected for changes in the output power of the FEL as a function of wavelength. The power output of the OPOs were sufficiently linear across the wavelength range of interest as to not require power correction. The measured IRMPD action spectra are only corrected for power within the scope of the individual spectrum and IRMPD yield values should not be compared directly. The IRMPD action spectra measured in the hydrogen-stretching region for the arabino nucleosides are expected to exhibit differences in relative intensities due to their acquisition on the QIT MS allowing for detection of small features when operating under reduced power/irradiation conditions to prevent saturation of more intense features.

2.3. Computational methods

Previous studies of the protonated canonical DNA and RNA nucleosides by IRMPD action spectroscopy highlighted several protonation sites that were potentially important [20–23]. For adenosine and 2′-deoxyadenosine, protonation at N1, N3, or N7 was found most favorable, and these sites of protonation were therefore studied for $[araAdo+H]^+$. The likely protonation sites for guanosine and 2′-deoxyguanosine were determined to be N3, N7, and O6, which are examined for $[araGuo+H]^+$. Study of protonated cytidine $[Cyd+H]^+$, and its DNA counterpart $[dCyd+H]^+$ concluded protonation at the N3 and O2 positions where both important, whereas studies of protonated uridine $[Urd+H]^+$, and 2′-deoxyuridine $[dUrd+H]^+$ found protonation at O2 and O4, as

well as protonation-induced tautomerization to the 2,4-dihydroxy tautomer favorable. A conformational search using a simulated annealing approach was performed using HyperChem 8.0 with the Amber 3 force field [35]. 1000 cycles of simulated annealing, from 0 K to 1000 K and back to 0 K over 0.8 ps, were performed for each unique protonation site (tautomeric state) for each arabinoside. The resulting structures were then sampled for unique conformations that were low in Gibbs energy. Approximately 50 of the most stable and unique structures for each protonation site were further analyzed by density functional theory (DFT) using Gaussian 09 [36]. Structures were first optimized using the B3LYP functional and a 6-311+G(d,p) basis set, after which vibrational frequencies were analyzed at the same level of theory. Single-point energy calculations were performed at the B3LYP/6-311+G(2d,2p) level of theory to further refine relative energetics. To aid in explanation of the presence of higher-energy conformers of $[araAdo+H]^+$ in the experiments, the effects of solvation on the relative stabilities of the ground and relevant excited conformers were examined by reoptimizing the structures, and then performing frequency analyses as well as single point energy calculations on the re-optimized structures in a polarizable continuum model (PCM) corresponding to water. The default PCM model provided in Gaussian, which uses the integral equation formalism variant (IEFPCM) was used [37].

The calculated vibrational frequencies for $[araAdo+H]^+$, $[araCyd+H]^+$, $[araGuo+H]^+$, and $[araUrd+H]^+$ were scaled by factors of 0.985, 0.978, 0.980, and 0.981 respectively, in the IR fingerprint region, and 0.955, 0.955, 0.961, and 0.957 respectively, in the hydrogen-stretching region, before comparison to the experimental data to provide the best overall match to the measured spectra. Vibrational frequencies in the IR fingerprint region were convoluted with a 20 cm^{-1} full-width at half-maximum (FWHM) Gaussian line shape to represent the width of measured features, whereas a 15 cm^{-1} FWHM Gaussian line shape was used in the hydrogen-stretching region. These calculations are harmonic in nature, and as such some disagreement is expected when comparing the predicted linear IR spectra to measured IRMPD spectra that have some inherent degree of anharmonicity. As the degree of anharmonicity present in each vibrational mode is unique, and influenced by changes in the local environment (e.g., resulting from protonation or hydrogen-bonding interactions), one might expect that each vibrational mode should require a unique scaling factor to account for the errors in estimating the resonant vibrational frequencies using the harmonic approximation. However, anharmonicities of similar vibrations can typically be accounted for by a single scaling factor achieving reasonable agreement with the measured spectrum. Vibrations in the IR fingerprint region in the nucleosides are sufficiently different from those in the hydrogen-stretching region as to require different scaling factors to reasonably correct for their anharmonicity. The scaling factors used were chosen to produce the best agreement with the measured spectrum without introducing bias from relative energetics or protonation site, exhibit only very minor variations, and correspond well to those used in prior studies of the protonated canonical DNA and RNA nucleosides.

Beyond the state of protonation, the structures are further described by several dihedral angles extracted from the calculations. The series of five dihedral angles defining the sugar ring are used to calculate a pseudorotation angle as set out by Altona and Sundaralingam [38]. This pseudorotation angle is used to precisely identify the sugar puckering as a specific envelope, E, or twisted, T, conformer, as these can be difficult to visually distinguish. Envelope structures are characterized by a single atom lying above or below the plane defined by the sugar ring, whereas twisted structures have two atoms puckered out of the plane, one above and one below, with one of those atoms puckered farther out-of-plane than the other. Atoms above the plane of the sugar ring are denoted with a superscript, whereas those below the plane are subscripted. Atoms puckered farther out-of-plane are noted to the left of the E/T designation, whereas those puckered less are indicated to the right of the designator. The common designations of nucleic acid sugar puckering, such as C2′-*endo* or C3′-*endo*, are defined within the more precise E and T conformers as a range that includes the ideal E conformer (C2′-*endo*, ^{2}E, or C3′-*endo*, ^{3}E for example), and the two T conformers closest to it in pseudorotation angle ($^2T_3$ and $^2T_1$ surround ^{2}E for example). The common designations used for nucleoside orientation: *anti*, where the nucleobase is oriented to facilitate Watson-Crick base pairing, and *syn*, facilitating Hoogsteen base pairing, are classified using the glycosidic bond dihedral angle, ∠O4′C1′N1C2 for pyrimidines and ∠O4′C1′N9C4 for purines, from the calculated structure.

3. Results

3.1. IRMPD action spectroscopy

Photodissociation of each protonated arabinoside led to loss of the protonated nucleobase via cleavage of the glycosidic bond as follows,

$$[araNuo + H]^+ + n\,h\nu \rightarrow [Nua + H]^+ + (araNuo - Nua) \quad (2)$$

where araNuo is the relevant arabinoside and Nua is the corresponding nucleobase. IRMPD action spectra of $[araAdo+H]^+$, $[araCyd+H]^+$, $[araGuo+H]^+$, and $[araUrd+H]^+$ are compared with those for the analogous protonated canonical DNA and RNA nucleosides to elucidate the influence of the 2′-substituents and stereochemistry on the spectral features. As can be seen in Fig. 2, the IRMPD spectrum of $[araAdo+H]^+$ exhibits a high degree of similarity to those previously measured for both $[Ado+H]^+$ and $[dAdo+H]^+$. Particularly in the IR fingerprint region, the relative intensities of the spectral features between ~1665 and ~1095 cm^{-1} are remarkably parallel to those of $[dAdo+H]^+$. Broadening/splitting of the feature centered at ~1080 cm^{-1} probably best differenti-

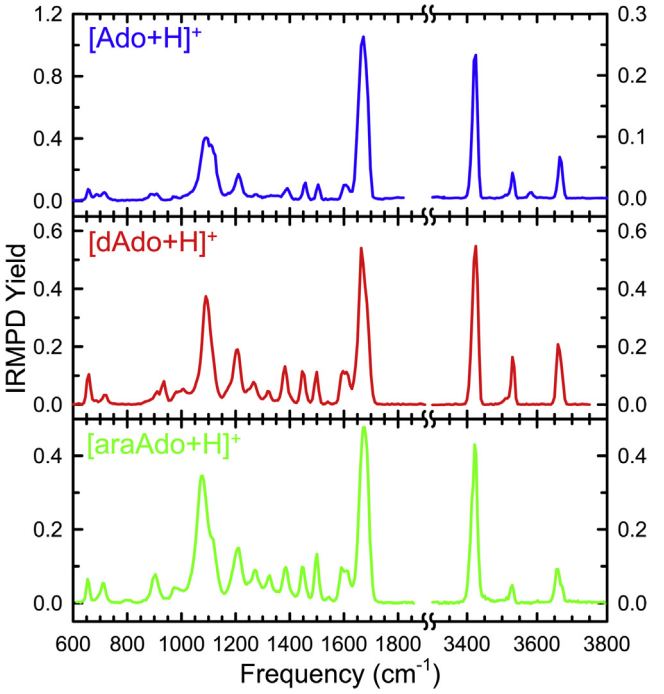

Fig. 2. Comparison of experimental IRMPD spectra of the protonated forms of the ribose, 2′-deoxyribose, and arabinose nucleosides of adenine in the IR fingerprint and hydrogen-stretching regions.

ates [araAdo+H]$^+$ from its canonical analogues in this region. In the hydrogen-stretching region [araAdo+H]$^+$ displays a small shoulder at ~3450 cm^{-1} that was not observed for either [Ado+H]$^+$ or [dAdo+H]$^+$, whereas [Ado+H]$^+$ displays a small feature at ~3580 cm^{-1}, attributed to its 2′-hydroxyl stretch, which is not observed in [dAdo+H]$^+$ or [araAdo+H]$^+$.

The measured IRMPD spectrum of [araCyd+H]$^+$ is parallel in peak position to those of both [Cyd+H]$^+$ and [dCyd+H]$^+$ (Fig. 3), but exhibits more extensive broadening and resembles most strongly that of [dCyd+H]$^+$ in terms of relative intensities in the IR fingerprint region. The small feature at ~1432 cm^{-1} in the spectrum of [araCyd+H]$^+$ is visible for [dCyd+H]$^+$, but is challenging to differentiate from noise in the spectrum of [Cyd+H]$^+$. The shape/broadening of the major feature at ~1100 cm^{-1} is more extensive for [araCyd+H]$^+$ than for [Cyd+H]$^+$ and [dCyd+H]$^+$ and probably best differentiates these nucleoside analogues in this region. In the hydrogen-stretching region the [araCyd+H]$^+$ feature at ~3450 cm^{-1} is more intense than the respective features of [Cyd+H]$^+$ and [dCyd+H]$^+$ and is blue-shifted by ~10 cm^{-1}. Conversely the ~3540 cm^{-1} feature of [Cyd+H]$^+$ and [dCyd+H]$^+$, attributed to asymmetric NH_2 stretches, appears diminished for [araCyd+H]$^+$. The feature at ~3575 cm^{-1} attributed to O2–H stretching in [dCyd+H]$^+$ and coupled O2–H and O2′–H stretching in [Cyd+H]$^+$, appears comparable in relative intensity for [araCyd+H]$^+$.

The IRMPD spectrum of [araGuo+H]$^+$ is comparable to those of both [Guo+H]$^+$ and [dGuo+H]$^+$ in peak positions (Fig. 4). The range between 3500 and 3600 cm^{-1} was re-examined for [araGuo+H]$^+$ with greater laser power to better define the small feature present there; this data is displayed in Fig. 4. In the IR fingerprint region [araGuo+H]$^+$ appears more like [dGuo+H]$^+$ in relative intensity with the feature at ~1640 cm^{-1} slightly below the intensity of the ~1795 cm^{-1} feature, and the relative intensities of the features between 1200 and 1500 cm^{-1} being more pronounced. Peak shapes in the IR fingerprint region are well reproduced between [araGuo+H]$^+$ and [dGuo+H]$^+$ and to a lesser extent [Guo+H]$^+$, although the feature at ~1100 cm^{-1} exhibits greater broadening/splitting than its canonical analogs. Peak positions in the hydrogen-stretching region of [Guo+H]$^+$ and [dGuo+H]$^+$ are generally well reproduced by [araGuo+H]$^+$, but a greater difference in the relative intensities is observed. In particular the intensity of the feature at ~3560 cm^{-1} is greatly reduced and the relative intensity of the large feature at ~3460 cm^{-1} appears to be much greater for [araGuo+H]$^+$ than measured for [Guo+H]$^+$ or [dGuo+H]$^+$. The substantial reduction in relative intensity for the feature at ~3560 cm^{-1} may be explained by the attribution of this feature in [Guo+H]$^+$ to the 2′-hydroxyl and NH_2 asymmetric stretches, the former of which might be expected to shift for [araGuo+H]$^+$.

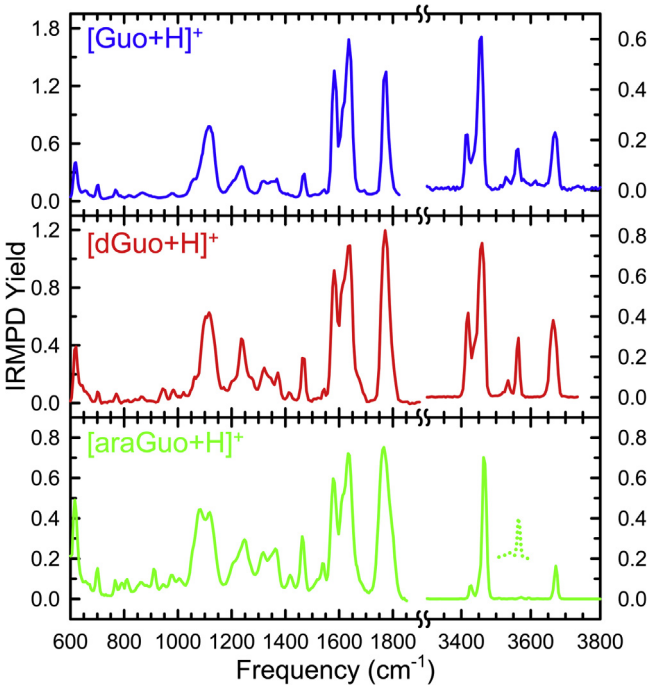

Fig. 4. Comparison of the experimental IRMPD spectra of the protonated forms of the ribose, 2′-deoxyribose, and arabinose nucleosides of guanosine in the IR fingerprint and hydrogen-stretching regions. Features of [araGuo+H]$^+$ recollected with greater laser power are overlaid and offset from the baseline to better illustrate these small features.

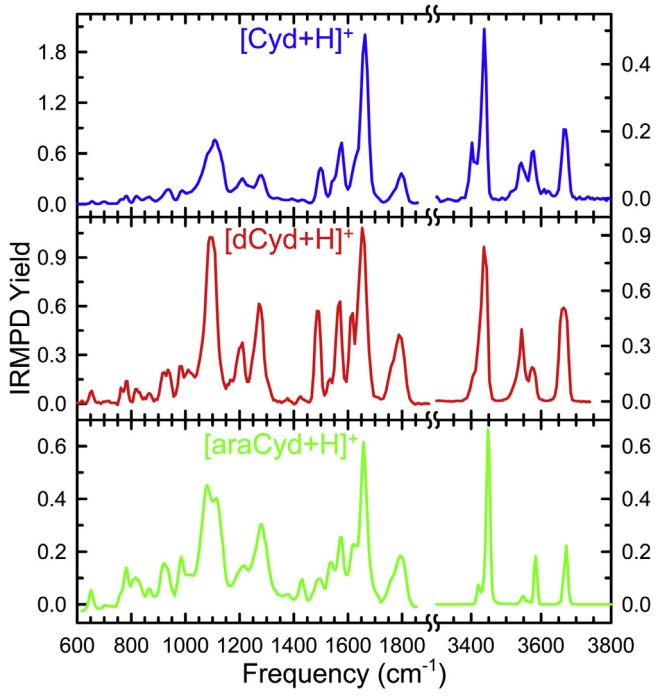

Fig. 3. Comparison of experimental IRMPD spectra of the protonated forms of the ribose, 2′-deoxyribose, and arabinose nucleosides of cytosine in the IR fingerprint and hydrogen-stretching regions.

The IRMPD spectrum of [araUrd+H]$^+$ corresponds very well in peak position to both those of [Urd+H]$^+$ and [dUrd+H]$^+$ (Fig. 5). The relative intensities of [araUrd+H]$^+$ appear to correspond better overall to those measured for [dUrd+H]$^+$, although the major features in the IR fingerprint region at ~1592 and ~1650 cm^{-1} display better agreement with those measured for [Urd+H]$^+$. The same broadening/splitting of the feature at ~1100 cm^{-1} is observed for [araUrd+H]$^+$ as for the other arabino nucleosides. Relative intensities in the hydrogen-stretching region of [araUrd+H]$^+$ appear more similar to those measured for [Urd+H]$^+$. In the hydrogen-stretching region the small feature at ~3511 cm^{-1} for [Urd+H]$^+$, attributed to O2′–H stretching, is not observed for [dUrd+H]$^+$ or [araUrd+H]$^+$. However, a small feature at ~3445 cm^{-1} is observed for [araUrd+H]$^+$ that does not appear in the spectra of [Urd+H]$^+$ or [dUrd+H]$^+$.

The near homology between the measured IRMPD spectra in the IR fingerprint region of the protonated arabino nucleosides with those of the protonated canonical DNA and RNA nucleosides suggests that stereochemical inversion of the 2′-position does not alter the protonation sites accessed from those found for the protonated forms of the canonical nucleosides. The broadening and splitting of the feature near ~1100 cm^{-1} is common to all four protonated arabino nucleosides and provides a means of differentiation from their canonical analogues. Shifting of at least one feature in each of

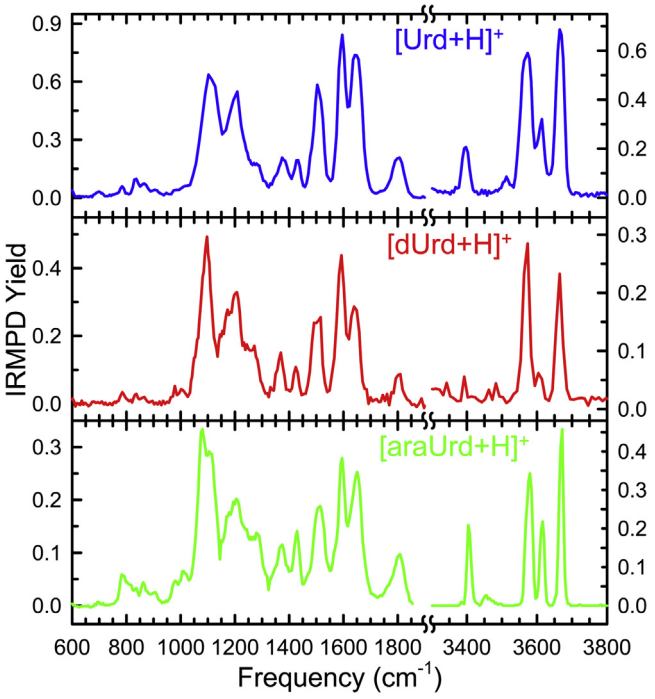

Fig. 5. Comparison of the experimental IRMPD spectra of the protonated forms of the ribose, 2′-deoxyribose, and arabinose nucleosides of uracil in the IR fingerprint and hydrogen-stretching regions.

the measured spectra in the hydrogen-stretching region however, suggests some change in hydrogen-bonding for each arabinoside versus its protonated canonical counterparts.

3.2. Theoretical results

Low-energy conformers calculated for [araAdo+H]$^+$, [araCyd+H]$^+$, [araGuo+H]$^+$, and [araUrd+H]$^+$ are shown in Figs. S1 through S4 of the Electronic Supplementary information, respectively. Conformations are designated based on the site of protonation, which is appended by an uppercase letter denoting its relative stability within the family of conformers computed for that site of protonation (with A representing the most stable conformer, B representing the next most stable conformer, etc.). Important structural parameters and relative Gibbs energies for the low-energy conformers of the protonated arabinosides are listed in Tables S1 through S4, and parallel data on the low-energy protonated RNA and DNA nucleoside conformers studied previously [20–23] are listed in Tables S5 through S8 for comparison. Low-energy conformers of [araAdo+H]$^+$ display a broad range of nucleobase orientations, predominately *syn* with *anti* oriented nucleobases more common slightly higher in Gibbs energy. Several less common sugar puckers are observed among the most stable conformers, such as C4′-*exo* and C1′-*exo*, though the more common C2′-*endo* sugar pucker is also observed in several low-energy conformers. C3′-*endo* sugar puckering is not observed in any conformer lying within 21 kJ/mol of the ground conformer. As with its canonical DNA and RNA counterparts [21], [araAdo+H]$^+$ prefers protonation at the N3-position. The calculated ground conformer, **N3A**$_{araAdo}$, is stabilized by an N3H$^+$···O5′ intramolecular hydrogen-bonding interaction, leading to a *syn* nucleobase orientation, similar to that found for the ground conformers calculated for its protonated DNA and RNA analogs. **N3A**$_{araAdo}$ and **N3B**$_{araAdo}$ display C4′-*exo* and C1′-*exo* sugar puckers respectively, but otherwise display the same hydrogen-bonding and nucleobase orientation. **N3C**$_{araAdo}$ is the lowest-energy conformer to display hydrogen-bonding interactions within the sugar, occurring through an N3H$^+$···O5′H···O2′ dual-hydrogen-bonding interaction, stabilizing a *syn* nucleobase orientation and lying only 2.7 kJ/mol higher in Gibbs energy, whereas **N3D**$_{araAdo}$ exhibits an N3H$^+$···O2′H···O5′ dual-hydrogen-bonding interaction and lies 3.8 kJ/mol higher in Gibbs energy. Both **N3C**$_{araAdo}$ and **N3D**$_{araAdo}$ display a C2′-*endo* sugar pucker. However, **N3D**$_{araAdo}$ displays a glycosidic bond angle of 90.7°, which by definition labels it with an *anti* nucleobase orientation, whereas it is more accurately described as *high syn* [39]. N1-protonated conformers are at least 18.3 kJ/mol higher in Gibbs energy and, lacking the N3H$^+$···O5′ or N3H$^+$···O2′ interactions to stabilize a *syn* nucleobase orientation, prefer an *anti* oriented nucleobase. **N1A**$_{araAdo}$ and **N1B**$_{araAdo}$ stabilize the sugar through an O2′H···O5′ hydrogen-bonding interaction, whereas the nucleobase is stabilized in an *anti* orientation by a noncanonical C8H···O4′ hydrogen-bonding interaction. **N1C**$_{araAdo}$ and **N1D**$_{araAdo}$ also display a noncanonical C8H···O5′ hydrogen-bonding interaction to stabilize an *anti* nucleobase orientation and a C3′-*endo* sugar pucker. Calculations in implicit water using a polarizable continuum model [37] for the lowest Gibbs energy **N3A**$_{araAdo}$ and **N1A**$_{araAdo}$ conformers indicate that in solution the **N1A**$_{araAdo}$ conformer is preferred by 1.8 kJ/mol. The most stable N7-protonated conformer **N7A**$_{araAdo}$ lies 29.6 kJ/mol higher in Gibbs energy than the ground conformer. **N7A**$_{araAdo}$, and **N7B**$_{araAdo}$, which lies merely 1.2 kJ/mol above **N7A**$_{araAdo}$, display the C8H···O5′ and O2′H···O5′ hydrogen-bonding interactions, respectively.

Low-energy conformers of [araCyd+H]$^+$ are broadly consistent with the low-energy conformers for [Cyd+H]$^+$ and [dCyd+H]$^+$ [23]. The calculated ground conformer **N3A**$_{araCyd}$ displays an O2′H···O5′ intramolecular hydrogen-bonding interaction stabilizing an *anti* nucleobase orientation and C2′-*endo* sugar pucker. **N3B**$_{araCyd}$, lying only 2.8 kJ/mol higher in Gibbs energy, displays a noncanonical C6H···O5′ hydrogen-bonding interaction also stabilizing an *anti* nucleobase orientation, but instead with a C3′-*endo* sugar pucker. **N3C**$_{araCyd}$ and **N3D**$_{araCyd}$ are 3′-hydroxyl rotamers of **N3A**$_{araCyd}$ and **N3B**$_{araCyd}$, respectively. The lowest energy O2-protonated conformer, **O2A**$_{araCyd}$, lies only 5.4 kJ/mol higher in Gibbs energy than **N3A**$_{araCyd}$, also displaying an O2′H···O5′ hydrogen-bonding interaction with an *anti* nucleobase orientation and C2′-*endo* sugar pucker. **O2B**$_{araCyd}$ is a 3′-hydroxyl rotamer of **O2A**$_{araCyd}$, whereas **O2C**$_{araCyd}$ displays the noncanonical C6H···O5′ hydrogen-bonding interaction with an *anti* nucleobase orientation and C3′-*endo* sugar pucker. The most stable conformer displaying a *syn* nucleobase orientation, **O2J**$_{araCyd}$, lies 19.9 kJ/mol higher in Gibbs energy, and is stabilized by a O2H···O2′H···O5′ dual-hydrogen-bonding interaction with a C1′-*exo* sugar pucker.

Low-energy conformers of [araGuo+H]$^+$ are consistent in protonation site with [Guo+H]$^+$ and [dGuo+H]$^+$ [20]. The calculated ground conformer of [araGuo+H]$^+$, **N7A**$_{araGuo}$, displays an O2′H···O5′ intramolecular hydrogen-bonding interaction stabilizing an *anti* nucleobase orientation and C2′-*endo* sugar pucker. Its 3′-hydroxyl rotamer, **N7B**$_{araGuo}$, lies only 1.7 kJ/mol higher in Gibbs energy. **N7C**$_{araGuo}$ and **N7D**$_{araGuo}$, 2′- and 3′-hydroxyl rotamers of one another, display a noncanonical C8H···O5′ hydrogen-bonding interaction stabilizing an *anti* nucleobase orientation and C3′-*endo* sugar puckering. The most stable conformer with a *syn* oriented nucleobase, **N7M**$_{araGuo}$, is stabilized by an O2′H···O5′H···N3 dual hydrogen-bonding interaction with C2′-*endo* sugar puckering. The most stable O6-protonated conformer, **O6A**$_{araGuo}$, displays O2′H···O5′ hydrogen-bonding with an *anti* nucleobase and C2′-*endo* sugar puckering and lies 38.2 kJ/mol higher in Gibbs energy. The most stable N3-protonated conformer, **N3A**$_{araGuo}$, lies 47.0 kJ/mol higher in Gibbs energy and stabilizes a *syn* nucleobase orientation by an N3H$^+$···O5′H···O2′H dual hydrogen-bonding interaction and displays C2′-*endo* sugar puckering.

The calculated protonation preference of [araUrd+H]$^+$ is different from that found for [Urd+H]$^+$ where a 2,4-dihydroxy tautomer is preferred with O4-protonated conformers found 2.9 kJ/mol higher in Gibbs energy, but is consistent with the calculated protonation preference for [dUrd+H]$^+$ [22]. In contrast, [araUrd+H]$^+$ prefers O4-protonation over the 2,4-dihydroxy tautomer **TA**$_{araUrd}$ by 3.9 kJ/mol, with **O4A**$_{araUrd}$ found to be the ground conformer. **O4A**$_{araUrd}$ and **TA**$_{araUrd}$ both display O2′H···O5′ hydrogen-bonding interactions stabilizing *anti* nucleobase orientations and C2′-*endo* sugar puckering. The lowest energy O2-protonated conformer, **O2A**$_{araUrd}$, displays an O2H$^+$···O2′H···O5′ dual hydrogen-bonding interaction stabilizing a *syn* nucleobase orientation and C1′-*exo* sugar pucker, and lies only 9.0 kJ/mol higher in Gibbs energy than **O4A**$_{araUrd}$. **O4B**$_{araUrd}$ and **TB**$_{araUrd}$ lie only 2.2 and 0.7 kJ/mol higher in Gibbs energy than their more stable counterparts, respectively, but are stabilized by noncanonical C6H···O5′ hydrogen-bonding interactions with *anti* nucleobase orientations and C3′-*endo* sugar puckering. The most stable conformer displaying an O2H$^+$···O5′ hydrogen-bonding interaction between the nucleobase and sugar, **O2C**$_{araUrd}$, was computed to be 28.8 kJ/mol higher in Gibbs energy than the **O4A**$_{araUrd}$ ground conformer, whereas a conformer exhibiting this interaction was calculated to be just 2.9 and 8.8 kJ/mol less stable than the ground conformers for [Urd+H]$^+$ and [dUrd+H]$^+$, respectively [22].

4. Discussion

4.1. Conformers accessed by [araAdo+H]$^+$

The measured IRMPD spectrum of [araAdo+H]$^+$ and calculated IR spectra of conformers relevant to the experiments are shown in Fig. 6. Additional comparisons with calculated low-energy conformers exhibiting unique structures are shown in Fig. S5 of the Electronic Supplementary information. Spectral regions displaying disagreement precluding the presence of the conformer in the experiments are highlighted. The calculated IR spectra of **N3A**$_{araAdo}$, **N3B**$_{araAdo}$, and **N3D**$_{araAdo}$ match the measured IRMPD spectrum in the hydrogen-stretching region well and display reasonable agreement with the IR fingerprint region. This agreement coupled with their calculated low Gibbs energies indicates that they are likely present in the experiments. Although computed to be 18.3 kJ/mol less stable than **N3A**$_{araAdo}$, **N1A**$_{araAdo}$ displays excellent agreement over both the IR fingerprint and hydrogen-stretching regions, with much better alignment for the small features observed between 1200 and 1500 cm^{-1} and better prediction of the relative intensities in the hydrogen-stretching region. The feature calculated at ~3450 cm^{-1} arises from the O2′–H stretch, which is directly involved in an O2′H···O5′ hydrogen bond, which may explain the significant reduction in the observed intensity versus that predicted by calculation. The distinctive N3–H$^+$ stretch found in **N3A**$_{araAdo}$ and **N3B**$_{araAdo}$ is predicted outside the frequency range of the measured spectrum. Likewise, the O2′–H stretch of **N3D**$_{araAdo}$ is also predicted outside of the measured spectrum. Relative energetics calculated in implicit water suggest that the **N1A**$_{araAdo}$ conformer is preferred over the **N3A**$_{araAdo}$ conformer by 1.8 kJ/mol in solution, suggesting kinetic trapping of this solution preferred conformer in the electrospray process. The broadening of the major feature observed at ~1675 cm^{-1} and the lack of distinctive major features unique to a given conformer or protonation site indicates that both N3- and N1- conformers are likely present. All other N1- and N3-protonated conformers exhibit shifting of at least one spectral feature that precludes their presence in the experiments. N3H$^+$···O5′ or O2′H···O5′ hydrogen-bonding interactions are present in each of the conformers populated in the experiments. **N7A**$_{araAdo}$ lies particularly high in Gibbs energy and displays stark disagreement with the IRMPD spectrum in the hydrogen stretching region (see Fig. S5), excluding any N7-protonated conformers from the experiments. **N3A**$_{araAdo}$ and **N3B**$_{araAdo}$ both display *syn* nucleobase orientations, whereas **N3D**$_{araAdo}$ exhibits a technically defined *anti* nucleobase orientation that is more accurately described as *high syn*. **N1A**$_{araAdo}$ exhibits a typical *anti* nucleobase orientation. **N3A**$_{araAdo}$ and **N3B**$_{araAdo}$, which possess N3H$^+$···O5′ hydrogen-bonding interactions, exhibit C4′-*exo* and C1′-*exo* sugar puckering, respectively. Whereas **N3D**$_{araAdo}$ and **N1A**$_{araAdo}$, which display O2′H···O5′ hydrogen-bonding, exhibit C2′-*endo* sugar puckering. Vibrational assignments for the experimental spectrum based on the **N3A**$_{araAdo}$, **N3B**$_{araAdo}$, **N3D**$_{araAdo}$, and **N1A**$_{araAdo}$ conformers are detailed in Table S9.

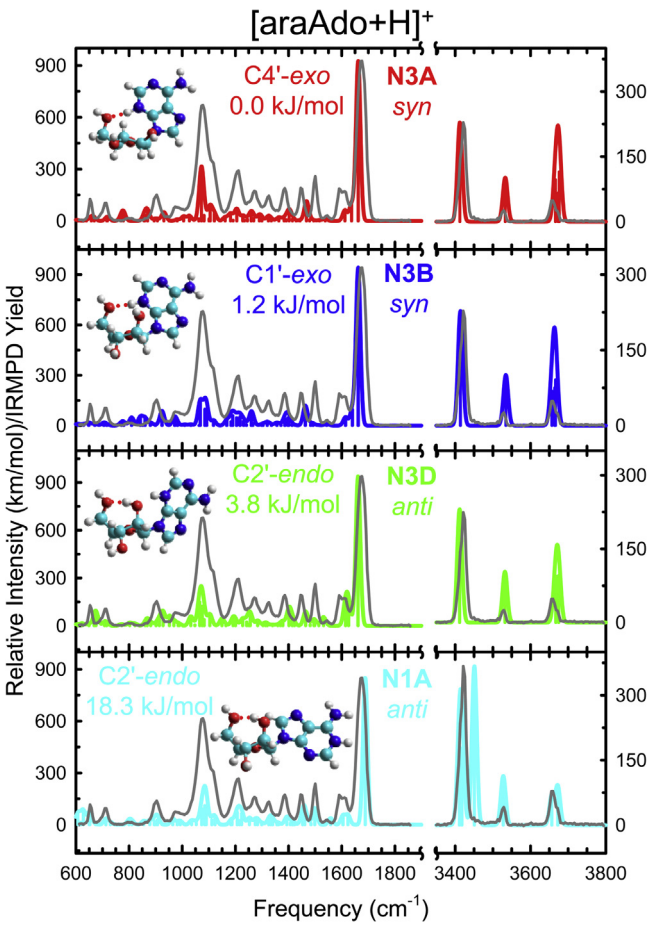

Fig. 6. Comparison of the measured IRMPD action spectrum of [araAdo+H]$^+$ with the B3LYP/6-311+G(d,p) predicted linear IR spectra for low-energy conformers of [araAdo+H]$^+$ populated in the experiments. Predicted vibrational frequencies are scaled by 0.985 and 0.955 in the IR fingerprint and hydrogen-stretching regions, respectively. Structural parameters including protonation site, nucleobase orientation, and sugar puckering, as well as relative B3LYP/6-311+G(2d,2p) Gibbs energies at 298 K are indicated. The measured IRMPD spectrum (shown in gray) is superimposed on the predicted IR spectrum and scaled to facilitate comparison.

4.2. Conformers accessed by [araCyd+H]$^+$

Comparisons of the measured IRMPD spectrum of [araCyd+H]$^+$ and calculated IR spectra for conformers relevant to the experimental spectrum and representative of the protonation sites studied are shown in Fig. 7. Additional comparisons with calculated low-energy conformers displaying unique structures are shown in Fig. S6 of the Electronic Supplementary information. Spectral regions displaying deviation excluding conformers from the experiments are highlighted. The predicted IR spectrum of the calculated ground conformer, **N3A**$_{araCyd}$, agrees well with the measured IRMPD spec-

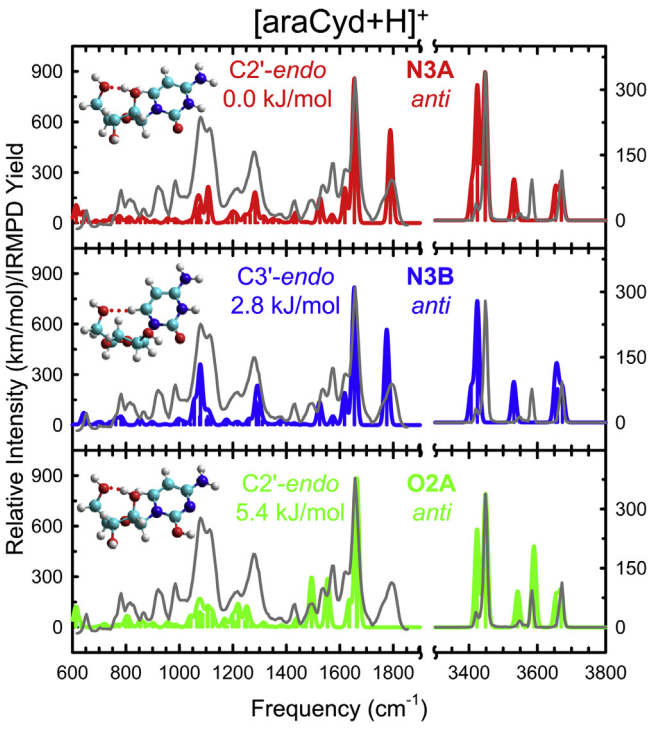

Fig. 7. Comparison of the measured IRMPD action spectrum of $[araCyd+H]^+$ with the B3LYP/6-311+G(d,p) predicted linear IR spectra for low-energy conformers of $[araCyd+H]^+$ populated in the experiments. Predicted vibrational frequencies are scaled by 0.978 and 0.955 in the IR fingerprint and hydrogen-stretching regions, respectively. Structural parameters including protonation site, nucleobase orientation, and sugar puckering, as well as relative B3LYP/6-311+G(2d,2p) Gibbs energies at 298 K are indicated. The measured IRMPD spectrum (shown in gray) is superimposed on the predicted IR spectrum and scaled to facilitate comparison.

trum in both the IR fingerprint and hydrogen-stretching regions. The calculated spectrum of **O2A**$_{araCyd}$ also agrees well with the measured IRMPD spectrum with better representation of features in the hydrogen-stretching region at 3550 and 3585 cm^{-1} and critically, features at 1500 and 1585 cm^{-1} complementary to those observed in the IR fingerprint region for **N3A**$_{araCyd}$. Based upon the major features at ~1657 and ~1803 cm^{-1} the N3 and O2 conformers appear to be present in roughly equal proportion indicating that, as found for previous studies of protonated cytidine [23,40], B3LYP may underestimate the stability of the O2-protonated conformer. Considering that **O2A**$_{araCyd}$ displays markedly better agreement, and notably less disagreement in the hydrogen-stretching region, suggests it may be more dominant in the experimental population than the IR fingerprint region alone would indicate. Both **N3A**$_{araCyd}$ and **O2A**$_{araCyd}$ display the unique O2′H···O5′ hydrogen-bonding interaction, and only conformers with this interaction are predicted to display the feature at ~3445 cm^{-1}, which corresponds to the most prominent peak observed in the hydrogen-stretching region. **N3B**$_{araCyd}$, which does not display O2′H···O5′ hydrogen-bonding, and displays C3′-*endo* sugar puckering with an *anti* nucleobase orientation, also displays reasonable agreement, but lacks the same splitting of the feature near ~1100 cm^{-1} observed in **N3A**$_{araCyd}$. Rotation of the 3′-hydroxyl groups in **N3A**$_{araCyd}$ and **N3B**$_{araCyd}$ produces **N3C**$_{araCyd}$ and **N3D**$_{araCyd}$ respectively, whose spectra are highly parallel (see Fig S6). **N3A**$_{araCyd}$ and its 3′-hydroxyl rotamer **N3C**$_{araCyd}$, **O2A**$_{araCyd}$, and potentially a small amount of **N3B**$_{araCyd}$ and its 3′-hydroxyl rotamer **N3D**$_{araCyd}$ are thus likely populated in the experiments. All other N3 and O2 protonated conformers display disagreement with at least one spectral feature precluding their presence in the experiments. These conformers encompass both O2′H···O5′ sugar-sugar or C6H···O5′ nucleobase-sugar hydrogen-bonding interactions. There appears to be an energetic and spectral preference for O2′H···O5′ (sugar–sugar) over C6H···O5′ (nucleobase–sugar) hydrogen–bonding interactions. All of these conformers exhibit *anti* nucleobase orientations. Those conformers displaying O2′H···O5′ hydrogen-bonding interactions also exhibit C2′-*endo* sugar puckering, whereas those that display C6H···O5′ hydrogen-bonding exhibit C3′-*endo* sugar puckering. Vibrational assignments for the experimental spectrum based on the **N3A**$_{araCyd}$, **N3B**$_{araCyd}$, and **O2A**$_{araCyd}$ conformers are detailed in Table S10.

4.3. Conformers accessed by $[araGuo+H]^+$

The measured IRMPD spectrum of $[araGuo+H]^+$ and calculated IR spectra of low-energy $[araGuo+H]^+$ conformers displaying good agreement are compared in Fig. 8. Additional comparisons with low-energy structures representing all protonation sites studied and unique structures are shown in Fig. S7 of the Electronic Supplementary information. Regions displaying discrepancy between the predicted and measured IRMPD spectrum indicating that the conformer is not populated in the experiments are highlighted. The **N7A**$_{araGuo}$ conformer, with an O2′H···O5′ hydrogen-bonding interaction, displays the best agreement in terms of both peak position and relative intensity in the IR fingerprint and hydrogen-stretching regions. The major features and most of the minor features are represented quite well by the spectrum of **N7A**$_{araGuo}$. The **N7B**$_{araGuo}$ conformer, a 3′-hydroxyl rotamer of **N7A**$_{araGuo}$, displays a highly parallel spectrum to **N7A**$_{araGuo}$ with only minor shifts in the IR fingerprint region in the shape of the complex feature centered at 1100 cm^{-1}, which displays less splitting, and a small feature at 1180 cm^{-1} that is not visible in the measured spectrum (see Fig. S7). Its overall reasonable agreement suggests that it may be present in the experiments, but these differences indicate that it is likely to be a less important contributor than **N7A**$_{araGuo}$. The **N7C**$_{araGuo}$ conformer, which displays a noncanonical C8H···O5′ hydrogen-bonding interaction between the nucleobase and sugar, also displays good agreement with the major features from 1400 to 1800 cm^{-1} and over the hydrogen-stretching region.

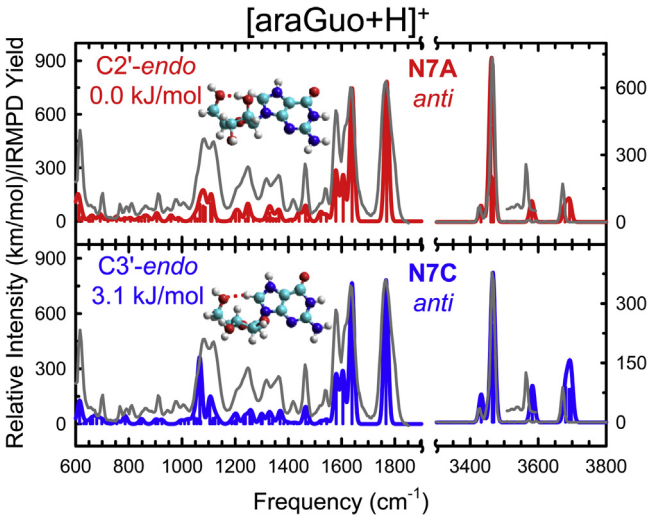

Fig. 8. Comparison of the measured IRMPD action spectrum of $[araGuo+H]^+$ with the B3LYP/6-311+G(d,p) predicted linear IR spectra for low-energy conformers of $[araGuo+H]^+$ populated in the experiments. Predicted vibrational frequencies are scaled by 0.980 and 0.961 in the IR fingerprint and hydrogen-stretching regions, respectively. Structural parameters including protonation site, nucleobase orientation, and sugar puckering, as well as relative B3LYP/6-311+G(2d,2p) Gibbs energies at 298 K are indicated. The measured IRMPD spectrum (shown in gray) is superimposed on the predicted IR spectrum and scaled to facilitate comparison. Features recollected with greater laser power are overlaid and offset from the baseline to better illustrate these small features.

However **N7C**$_{araGuo}$ displays greater discrepancy in the unresolved features around ~1100 cm^{-1} in both position and relative intensities of the two features. The notably higher-energy **O6A**$_{araGuo}$ conformer displays greater disagreement in both regions (see Fig. S7), but the small shoulder measured at ~1690 cm^{-1} corresponds well to a major feature predicted for the O6-protonated conformers suggesting **O6A**$_{araGuo}$ may be present in small abundance in the experiments. Other O6-protonated conformers lying higher still in Gibbs energy display more significant disagreement with the measured IRMPD spectrum, indicating they are not present in the experiments. Higher-energy N7- and N3-protonated conformers all display at least one spectral feature in disagreement with the measured spectrum excluding their presence from the experiments. **N3A**$_{araGuo}$ and other N3-protonated conformers display notable disagreement with both major and minor features of the measured spectrum (see Fig. S7), indicating they are not present in the experiments. **N7A**$_{araGuo}$ and **N7B**$_{araGuo}$ display C2′-*endo* sugar puckering stabilized by O2′H···O5′ hydrogen-bonding interactions and *anti* nucleobases, whereas **N7C**$_{araGuo}$ displays C3′-*endo* sugar puckering and an *anti* nucleobase orientation. Vibrational assignments for the experimental spectrum based on the **N7A**$_{araGuo}$, **N7B**$_{araGuo}$, and **N7C**$_{araGuo}$ conformers are detailed in Table S11.

4.4. Conformers accessed by [araUrd+H]$^+$

The measured IRMPD spectrum of [araUrd+H]$^+$ and conformers relevant to the experiments are compared in Fig. 9. Additional comparisons including all of the studied protonation sites and examples of all unique structures calculated are shown in Fig. S8 of the Electronic Supplementary information. Spectral regions demonstrating disagreement with the measured IRMPD spectrum, eliminating the corresponding conformer from the experiments, are highlighted. The predicted IR spectra for **O4A**$_{araUrd}$, **O4B**$_{araUrd}$, **O4C**$_{araUrd}$ (a 3′-hydroxyl rotamer of **O4A**$_{araUrd}$), and **TA**$_{araUrd}$ match the measured spectrum reasonably well in both the IR fingerprint and hydrogen-stretching regions. Critically, the O4 and T conformers are complementary to one another, with several unique diagnostic features for O4 conformers at ~1800, ~3410, and ~3610 cm^{-1}, and several features unique to T conformers at ~1660 and ~3570 cm^{-1} that indicate comparable populations of the O4 and T conformers in the experiments. Also useful is the feature at ~3455 cm^{-1}, which is unique to conformers displaying the O2′H···O5′ hydrogen-bonding interaction. Amongst these conformers, only **O4B**$_{araUrd}$ does not exhibit the O2′H···O5′ hydrogen-bonding interaction, but the small feature unique to this conformer at ~1025 cm^{-1} indicates that it is likely present in the experiments. **O2A**$_{araUrd}$ exhibits greater differences with the measured spectrum (see Fig. S8), particularly with the major features between 1550 and 1700 cm^{-1}, precluding it from notable presence in the experiments. **O4A**$_{araUrd}$, **O4C**$_{araUrd}$, and **TA**$_{araUrd}$, all of which have an O2′H···O5′ hydrogen-bonding interaction, all exhibit C2′-*endo* sugar puckering, whereas **O4B**$_{araUrd}$ exhibits C3′-*endo* sugar puckering. All of the populated conformers exhibit *anti* nucleobase orientations. **O2A**$_{araUrd}$, precluded from the experimental population, is the most stable conformer exhibiting a *syn* nucleobase orientation. All higher-energy O2 and O4-protonated as well as T conformers are excluded from the experimentally accessed population by disagreement with at least one spectral feature. Vibrational assignments for the experimental spectrum based on the **O4A**$_{araUrd}$, **O4B**$_{araUrd}$, **O4C**$_{araUrd}$, and **TA**$_{araUrd}$ conformers are detailed in Table S12.

4.5. Effect of Inversion of the 2′ Stereochemistry on the Conformations of [araNuo+H]$^+$

In the absence of a stronger intramolecular interaction stabilizing the sugar and nucleobase, such as the N3H$^+$···O5′

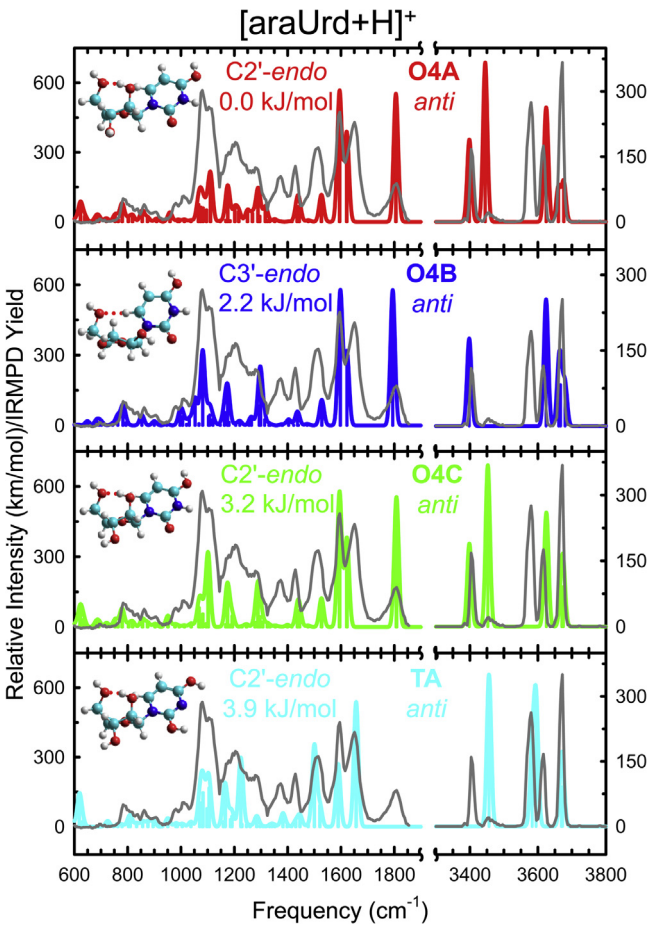

Fig. 9. Comparison of the measured IRMPD action spectrum of [araUrd+H]$^+$ with the B3LYP/6-311+G(d,p) predicted linear IR spectra for low-energy conformers of [araUrd+H]$^+$ populated in the experiments. Predicted vibrational frequencies are scaled by 0.981 and 0.957 in the IR fingerprint and hydrogen-stretching regions, respectively. Structural parameters including protonation site, nucleobase orientation, and sugar puckering, as well as relative B3LYP/6-311+G(2d,2p) Gibbs energies at 298 K are indicated. The measured IRMPD spectrum (shown in gray) is superimposed on the predicted IR spectrum and scaled to facilitate comparison.

hydrogen-bonding interaction calculated to be preferred and spectroscopically determined to be important in [araAdo+H]$^+$, inversion of the stereochemistry at the 2′-position results in a calculated preference for stabilization of the sugar puckering as C2′-*endo* through an O2′H···O5′ hydrogen-bonding interaction. However for [araAdo+H]$^+$, the higher-energy **N1A**$_{araAdo}$ conformer, which does display the O2′H···O5′ hydrogen-bonding interaction, matches the measured spectrum quite well suggesting it is also important in the experiments. The presence of both N3- and N1-protonated conformers of [araAdo+H]$^+$ in the experiments is in agreement with the protonation sites found for [Ado+H]$^+$ and [dAdo+H]$^+$. Sugar puckerings populated shift from C2′-*endo* and C3′-*endo* in [Ado+H]$^+$ and [dAdo+H]$^+$ to C4′-*exo*, C1′-*exo*, and C2′-*endo* in [araAdo+H]$^+$. The nucleobase orientations of the N3 and N1 protonated conformers remain consistent as *syn* and *anti*, respectively. [araCyd+H]$^+$ displays extremely parallel structures to those found for [Cyd+H]$^+$ and [dCyd+H]$^+$, the primary difference being the presence of the O2′H···O5′ hydrogen-bonding interaction. The calculated stabilities of the N3 and O2-protonated conformers are similar to those found for [Cyd+H]$^+$ and [dCyd+H]$^+$, and *anti* nucleobase orientations with either C2′-*endo* or C3′-*endo* sugar puckering remain consistent. Inversion of the 2′ stereochemistry imposes a heavier energetic penalty on *syn*-oriented nucleobases, with the most stable [araCyd+H]$^+$ conformer exhibiting a *syn* nucleobase orientation

found 12.5 and 9.6 kJ/mol higher in Gibbs energy than for $[Cyd+H]^+$ and $[dCyd+H]^+$ respectively, and remains unpopulated in the experiments. The conformers of $[araGuo+H]^+$, with predominately N7-protonated conformers populated, are also in excellent agreement with those found for $[Guo+H]^+$ and $[dGuo+H]^+$. The exception to this being the O2′H···O5′ hydrogen-bonding interaction taking precedence over the noncanonical C8H···O5′ nucleobase–sugar hydrogen bonding. This interaction does not change the preferred *anti* nucleobase orientation and both C2′-*endo* and C3′-*endo* sugar puckering are again present in the experiments. The conformers populated in the IRMPD experiments for $[araUrd+H]^+$ generally agree with those for $[Urd+H]^+$ and $[dUrd+H]^+$, being a mixture of O4 and T conformers. However the calculated preference for the O4-protonated versus T forms is inverted from that found for $[Urd+H]^+$, and more consistent with that found for $[dUrd+H]^+$, with the O4-protonated ground conformer calculated to be 3.9 kJ/mol more stable than the lowest-energy T conformer. Sugar puckerings populated in the experiments remain C2′-*endo* and C3′-*endo* across $[araUrd+H]^+$, $[dUrd+H]^+$, and $[Urd+H]^+$. The most stable conformers populated for each system exhibit *anti* nucleobase orientations, however higher energy *syn* conformers are populated in $[dUrd+H]^+$ and $[Urd+H]^+$, whereas no *syn* conformers appear to be populated for $[araUrd+H]^+$.

The presence of the 2′-hydroxyl moiety above the sugar ring in the arabino nucleosides would be expected to impose a steric restraint on the rotation of the nucleobase about the glycosidic bond versus that found in the canonical nucleosides. Glycosidic bond angles were extracted from all low-energy structures found within 20 kJ/mol of the ground conformer for the arabinosides and corresponding RNA and DNA nucleosides. These glycosidic bond angles are compared between the analogous protonated nucleosides in Fig. 10. Gibbs energies and structural parameters for

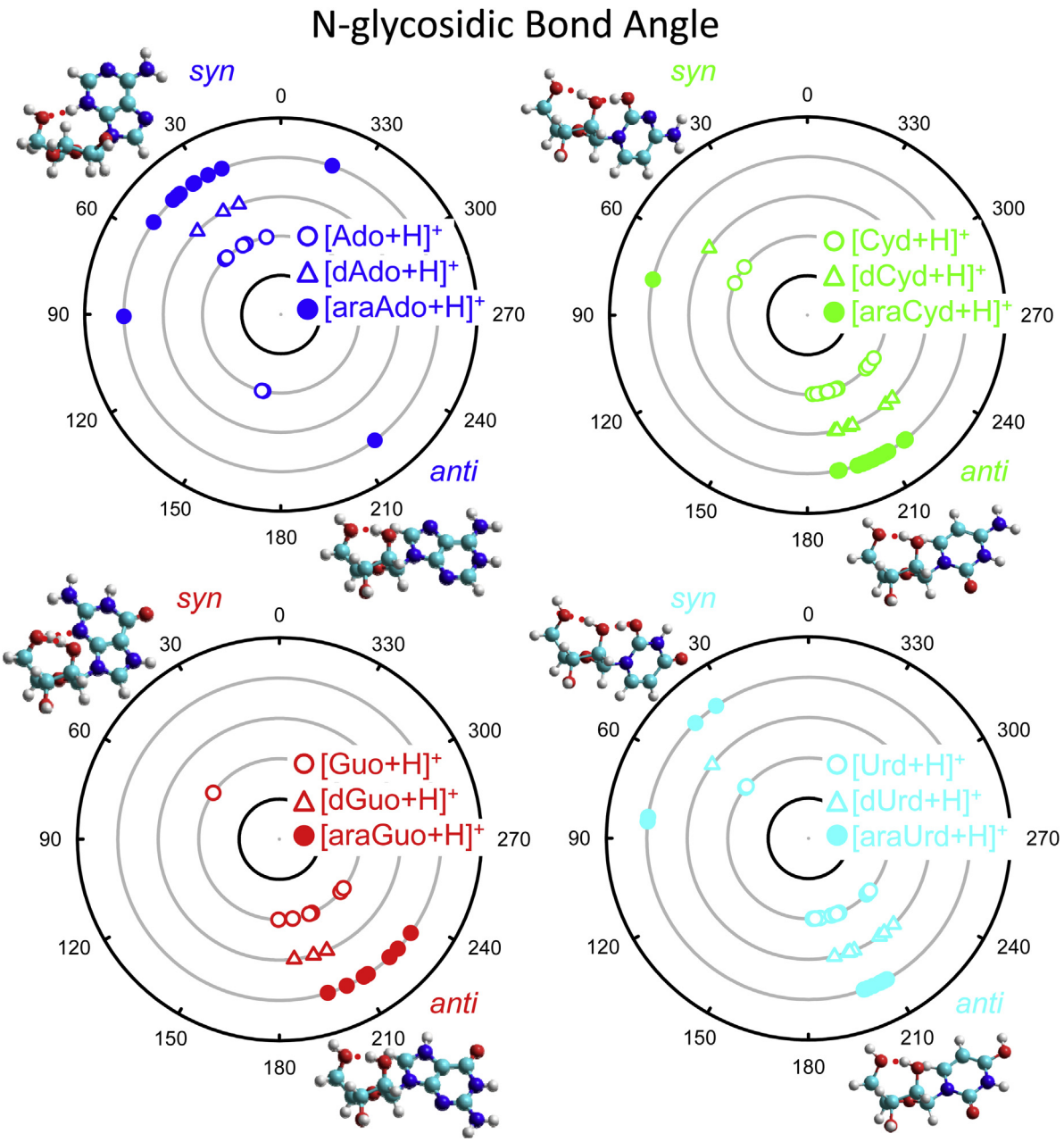

Fig. 10. Comparison of the glycosidic bond angles found in stable structures of the protonated RNA, DNA, and arabino nucleosides calculated within 20 kJ/mol Gibbs energy of the ground conformers. Examples of representative conformers exhibiting *syn* and *anti* nucleobase orientations are shown for each comparison.

the protonated arabinosides are listed in Tables S1–S4, and the Gibbs energies and structural parameters for the protonated DNA and RNA nucleosides are listed in Tables S5–S8 for comparison. For the pyrimidines, a narrower distribution of glycosidic bond angles is found in the arabinosides, particularly for [araUrd+H]$^+$ in which most of the calculated conformers within 20 kJ/mol in Gibbs energy are found in a narrow range of glycosidic bond angles centered at ∼205°. In [Urd+H]$^+$ however, it appears as though two distributions are observed. The conformers having glycosidic bond angles of ∼194° in [Urd+H]$^+$ and [Cyd+H]$^+$ have an O2H···O2′H···O3′ dual hydrogen-bonding interaction. In contrast, those conformers of [dCyd+H]$^+$ and [dUrd+H]$^+$ with glycosidic bond angles of ∼198° display a O3′H···O5′ hydrogenbonding interaction. The location of the 2′-hydroxyl moiety in the arabinosides makes the dual-hydrogen-bonding interaction less stabilizing, placing the conformers displaying it outside of the 20 kJ/mol window shown in Fig. 10, and the strong hydrogen bonding to O5′ similarly increases the relative barrier to rotation that would enable an O3′H···O5′ hydrogen-bonding interaction. The distribution of *anti* glycosidic bond angles for [araCyd+H]$^+$ and [araUrd+H]$^+$, centered at ∼205°, is different than that found for [Cyd+H]$^+$ and [Urd+H]$^+$, which is centered at ∼194°. This change is reflected by the subtle rotation of the nucleobase placing the C6–H atom closer to O4′ in [araCyd+H]$^+$ and [araUrd+H]$^+$. The range of glycosidic bond angles accessed by low-energy conformers of [araGuo+H]$^+$ is very similar to that of [Guo+H]$^+$, perhaps in part due to the larger number of conformers present below 20 kJ/mol relative Gibbs energy. Conversely, the range of glycosidic bond angles accessed by [dGuo+H]$^+$ in the same range is substantially smaller, perhaps again due to the extremely limited conformers present within this Gibbs energy range. The conformers calculated for [araAdo+H]$^+$ below 20 kJ/mol display a much wider range of glycosidic bond angles than those for [Ado+H]$^+$. The two *anti*-nucleobase conformers of [Ado+H]$^+$ in this energy range display a N3H$^+$···O2′H···O3′ dual-hydrogen-bonding interaction, which is not available to [araAdo+H]$^+$. The *anti* conformer calculated for [araAdo+H]$^+$, **N1A**$_{araAdo}$, displays the noncanonical C8H···O5′ hydrogen-bonding interaction. In contrast to this difference in *anti* conformers, the *syn* conformers are very parallel to those for [Ado+H]$^+$. The notably fewer conformers of [dAdo+H]$^+$ found within the 20 kJ/mol relative Gibbs energy range display a similar range in *syn* glycosidic bond angles, but the most stable N1 conformer, with an *anti* nucleobase orientation, is just beyond the 20 kJ/mol cut-off displayed.

5. Conclusions

Complimentary theoretical calculations and IRMPD action spectroscopy experiments of the protonated arabino nucleosides indicate that the preferred sites of protonation are preserved versus that found for the DNA and RNA nucleoside analogues, except for [araUrd+H]$^+$. However, the protonated uridine nucleoside analogues all exhibit populations that are mixtures of minor 2,4-dihydroxy tautomers and O4-protonated conformers. The protonation preference of [araUrd+H]$^+$ agrees with that of [dUrd+H]$^+$, which differs from the preference for the minor 2,4-dihydroxy tautomer over O4 protation found in [Urd+H]$^+$. As noted for [Ado+H]$^+$ and [dAdo+H]$^+$, kinetic trapping of the N1-protonated form of [araAdo+H]$^+$ is also observed. The presence of the 2′-hydroxyl moiety above the plane of the sugar ring alters the preferred sugar puckering mode for [araAdo+H]$^+$ and [araGuo+H]$^+$ to C4′-*exo* and C2′-*endo*, respectively, versus the C2′-*endo* and C3′-*endo* sugar puckerings preferred by their DNA and RNA counterparts. The theoretical calculations and IRMPD action spectroscopy studies of the protonated arabinosides also indicate the presence of an alternative mode of hydrogen-bonding not found in their canonical analogues via an O2′H···O5′ interaction in at least one of the conformers populated for each of the protonated arabinosides in the experiments. The ground conformers calculated for [araCyd+H]$^+$, [araGuo+H]$^+$, and [araUrd+H]$^+$ each display the O2′H···O5′ hydrogen-bonding interaction with stabilization of the nucleobase through an indirect interaction between C6–H of [araCyd+H]$^+$ and [araUrd+H]$^+$, and C8–H of [araGuo+H]$^+$, with O4′ providing additional stability for the nucleobase. The N3H$^+$···O5′ interaction of [araAdo+H]$^+$, also found in [Ado+H]$^+$ and [dAdo+H]$^+$, is calculated to provide greater stability through this nucleobase–sugar hydrogen-bonding interaction than the sugar–sugar hydrogen-bonding interaction. However, comparison with the measured spectrum indicates that the O2′H···O5′ hydrogen-bonding is also present in the experimentally accessed conformers due to **N3D**$_{araAdo}$ and **N1A**$_{araAdo}$. These results indicate that sugar–sugar stabilizing interactions are in direct competition with nucleobase–sugar interactions, revealing that stabilizing the flexible sugar puckering is competitive, and in all systems studied except [araAdo+H]$^+$, provides greater overall stability than stabilizing the nucleobase orientation about the glycosidic bond. The change in intramolecular hydrogen-bonding interactions for [araCyd+H]$^+$, [araGuo+H]$^+$, and [araUrd+H]$^+$ is accompanied by a shift in the glycosidic bond angles for low-energy conformers. Whereas [araAdo+H]$^+$, retaining largely the same hydrogen-bonding interaction in the Gibbs energy range shown, does not display a similar shift in glycosidic bond angles.

Acknowledgements

Financial support for this work was provided by the National Science Foundation, grant numbers OISE-0730072 and OISE-1357887 (for the FEL IRMPD measurements and international travel), DBI-0922819 (for the Bruker amaZon ETD quadrupole ion trap mass spectrometer), and CHE-1709789 (for other research costs). We gratefully acknowledge the Nederlandse Organisatie voor Wetenschappelijk Onderzoek (NWO) for the support of the FELIX Laboratory. L.A.H, C.C.H., and Z.J.D gratefully acknowledge support from Wayne State University Thomas C. Rumble Graduate Fellowships. Z.J.D. also gratefully acknowledges support from the Joseph Jasper Scholarship for Graduate Students in Chemistry. C.C.H. gratefully acknowledges Wayne State University for support from a summer dissertation fellowship. Computational resources and support for this work were provided by Wayne State University C&IT. The assistance of the skilled FELIX staff is immensely appreciated.

Appendix A. Supplementary data

Supplementary data associated with this article can be found, in the online version, at https://doi.org/10.1016/j.ijms.2019.01.005.

References

[1] H.E. Kaufman, C. Dohlman, E.L. Martola, Use of 5-Iodo-2'-deoxyuridine (IDU) in treatment of herpes simplex keratitis, Arch. Ophthalmol.-Chic. 68 (1962) 235–239.
[2] H.E. Kaufman, C. Heidelberger, Therapeutic antiviral action of 5-trifluoromethyl-2′-deoxyuridine in herpes simplex keratitis, Science 145 (1964) 585–586.
[3] F.M. Schabel, Antiviral activity of 9-beta-D-arabinofuranosyladenine (Ara-A), Chemotherapy 13 (1968) 321–338.
[4] W. Bergmann, D.C. Burke, Contributions to the study of marine products. XXXIX. The nucleosides of sponges. III. Spongothymidine and spongouridine, J. Org. Chem. 20 (1955) 1501–1507.
[5] W. Bergmann, R.J. Feeney, Contributions to the study of marine products. XXXII. The nucleosides of sponges. I, J. Org. Chem. 16 (1951) 981–987.
[6] E. Frei, J.N. Bickers, J.S. Hewlett, M. Lane, W.V. Leary, R.W. Talley, Dose schedule and antitumor studies of arabinosyl cytosine (NSC 63878), Cancer Res. 29 (1969) 1325–1332.
[7] C.K. Mathews, DNA synthesis as a therapeutic target: the first 65 years, FASEB J. 26 (2012) 2231–2237.

[8] A. Abraham, A.J. Devasia, S. Varatharajan, S. Karathedath, P. Balasubramanian, V. Mathews, Effect of cytosine arabinoside metabolizing enzyme expression on drug toxicity in acute myeloid leukemia, Ann. Hematol. 94 (2015) 883–885.
[9] M.J. Absalon, F.O. Smith, Treatment strategies for pediatric acute myeloid leukemia, Expert. Opin. Pharmaco. 10 (2009) 57–79.
[10] P.A. Cullis, R. Cushing, Vidarabine encephalopathy, J. Neurol. Neurosur. PS 47 (1984) 1351–1354.
[11] M. Pastor-Anglada, A. Felipe, F.J. Casado, Transport and mode of action of nucleoside derivatives used in chemical and antiviral therapies, Trends Pharmacol. Sci. 19 (1998) 424–430.
[12] W. Shen, J.S. Kim, P.E. Kish, J. Zhang, S. Mitchell, B.G. Gentry, J.M. Breitenbach, J.C. Drach, J. Hilfinger, Design and synthesis of vidarabine prodrugs as antiviral agents, Bioorg. Med. Chem. Lett. 19 (2009) 792–796.
[13] M. Hubert-Habart, S.S. Cohen, The toxicity of 9-beta-D-arabinofuranosyladenine to purine-requiring Escherichia coli, Biochim. Biophys. Acta 59 (1962) 468–471.
[14] S. Grant, Ara-C: cellular and molecular pharmacology, Adv. Cancer Res. 72 (1998) 197–233.
[15] J.G. Dalton, A.L. George, F.E. Hruska, T.N. McGaig, K.K. Ogilvie, J. Pelling, D.J. Wood, Comparison of arabinose and ribose nucleoside conformation in aqueous and dimethylsulfoxide solution. 2',5'-hydrogen bonding in arabinonucleosides, Biochim. Biophys. Acta 478 (1977) 261–273.
[16] F.E. Hruska, D.J. Wood, T.N. McCaig, A.A. Smith, A. Holy, A nuclear magnetic resonance study of nucleoside conformation in solution. The effect of structure and conformation on the magnetic nonequivalence of the 5′-methylene hydrogens, Can. J. Chem. 52 (1974) 497–508.
[17] P. Tollin, H.R. Wilson, D.W. Young, The molecular conformation of uracil-β-D-arabinofuranoside, Nat. New Biol. 242 (1973) 49–50.
[18] A.K. Chwang, M. Sundaralingam, S. Hanessian, Crystal and molecular structure of a purine arabinonucleoside, 9-β-D-arabinofuranosyladenine hydrochloride, Acta Crystallogr. B 30 (1974) 2273–2277.
[19] A. Saran, B. Pullman, D. Perahia, Molecular orbital calculations on the conformation of nucleic acids and their constituents. X. Conformation of beta-D-arabinosyl nucleosides, Biochim. Biophys. Acta 349 (1974) 189–203.
[20] R.R. Wu, B. Yang, G. Berden, J. Oomens, M.T. Rodgers, Gas-phase conformations and energetics of protonated 2'-deoxyguanosine and guanosine: IRMPD action spectroscopy and theoretical studies, J. Phys. Chem. B 118 (2014) 14774–14784.
[21] R.R. Wu, B. Yang, G. Berden, J. Oomens, M.T. Rodgers, Gas-phase conformations and energetics of protonated 2'-deoxyadenosine and adenosine: IRMPD action spectroscopy and theoretical studies, J. Phys. Chem. B 119 (2015) 2795–2805.
[22] R.R. Wu, B. Yang, C.E. Frieler, G. Berden, J. Oomens, M.T. Rodgers, Diverse mixtures of 2,4-dihydroxy tautomers and O4 protonated conformers of uridine and 2'-deoxyuridine coexist in the gas phase, Phys. Chem. Chem. Phys. 17 (2015) 25978–25988.
[23] R.R. Wu, B. Yang, C.E. Frieler, G. Berden, J. Oomens, M.T. Rodgers, N3 and O2 protonated tautomeric conformations of 2'-deoxycytidine and cytidine coexist in the gas phase, J. Phys. Chem. B 119 (2015) 5773–5784.
[24] R.R. Wu, B. Yang, C.E. Frieler, G. Berden, J. Oomens, M.T. Rodgers, 2,4-dihydroxy and O2 protonated tautomers of dThd and Thd coexist in the gas phase: methylation alters protonation preferences versus dUrd and Urd, J. Am. Soc. Mass Spectrom. 2 (2016) 410–421.
[25] Y. Zhu, L.A. Hamlow, C.C. He, H.A. Roy, N.A. Cunningham, M.U. Munshi, G. Berden, J. Oomens, M.T. Rodgers, Conformations and N-glycosidic bond stabilities of sodium cationized 2′-deoxycytidine and cytidine: solution conformation of $[Cyd+Na]^+$ is preserved upon ESI, Int. J. Mass Spectrom. 429 (2018) 18–27.
[26] Y. Zhu, L.A. Hamlow, C.C. He, S.F. Strobehn, J.K. Lee, J. Gao, G. Berden, J. Oomens, M.T. Rodgers, Influence of sodium cationization versus protonation on the gas-phase conformations and glycosidic bond stabilities of 2′-deoxyadenosine and adenosine, J. Phys. Chem. B 120 (2016) 8892–8904.
[27] Y. Zhu, L.A. Hamlow, C.C. He, J.K. Lee, J. Gao, G. Berden, J. Oomens, M.T. Rodgers, Gas-phase conformations and N-glycosidic bond stabilities of sodium cationized 2'-deoxyguanosine and guanosine: sodium cations preferentially bind to the guanine residue, J. Phys. Chem. B 121 (2017) 4048–4060.
[28] Y. Zhu, H.A. Roy, N.A. Cunningham, S.F. Strobehn, J. Gao, M.U. Munshi, G. Berden, J. Oomens, M.T. Rodgers, Effects of sodium cationization versus protonation on the conformations and N-glycosidic bond stabilities of sodium cationized uridine and 2′-deoxyuridine: solution conformation of $[Urd+Na]^+$ is preserved upon ESI, Phys. Chem. Chem. Phys. 19 (2017) 17637–17652.
[29] Y. Zhu, H.A. Roy, N.A. Cunningham, S.F. Strobehn, J. Gao, M.U. Munshi, G. Berden, J. Oomens, M.T. Rodgers, IRMPD action spectroscopy, ER-CID experiments, and theoretical studies of sodium cationized thymidine and 5-methyluridine: kinetic trapping during the ESI desolvation process preserves the solution structure of $[Thd+Na]^+$, J. Am. Soc. Mass Spectrom. 28 (2017) 2423–2437.
[30] N.C. Polfer, J. Oomens, D.T. Moore, G. von Helden, G. Meijer, R.C. Dunbar, Infrared spectroscopy of phenylalanine Ag(I) and Zn(II) complexes in the gas phase, J. Am. Chem. Soc. 128 (2006) 517–525.
[31] N.C. Polfer, J. Oomens, Reaction products in mass spectrometry elucidated with infrared spectroscopy, Phys. Chem. Chem. Phys. 9 (2007) 3804–3817.
[32] D. Oepts, A.F.G. van der Meer, P.W. van Amersfoort, The free-electron-laser user facility FELIX, Infrared Phys. Technol. 36 (1995) 297–308.
[33] J. Martens, G. Berden, C.R. Gebhardt, J. Oomens, Infrared ion spectroscopy in a modified quadrupole ion trap mass spectrometer at the FELIX free electron laser laboratory, Rev. Sci. Instrum. 87 (2016) 103108.
[34] L.A. Hamlow, Y. Zhu, Z.J. Devereaux, N.A. Cunningham, G. Berden, J. Oomens, M.T. Rodgers, Modified quadrupole ion trap mass spectrometer for infrared ion spectroscopy: application to protonated thiated uridines, J. Am. Soc. Mass Spectrom. 29 (2018) 2125–2137.
[35] K. Wolinski, J.F. Hinton, D.S. Wishart, B.D. Sykes, F.M. Richards, A. Pastone, V. Saudek, P.D. Ellis, G.E. Maciel, J.W. McIver Jr., A.C. Blizzard, D.P. Santry, J.A. Pople, N.S. Ostlund, L. Ducasse, J. Hoarau, M. Pesquer, M. Kondo, I. Ando, R. Chujo, A. Nishioka, E.C. Vauthier, S. Odiot, F. Tonnard, J.D. Baker, M.C. Zerner, D.V. Beveridge, W.P. Anderson, T.R. Cundari, R.C. Bingham, M.J.S. Dewar, D.H. Lo, J. Li, P.C. Mello, K. Jug, W. Thiel, E.G. Zoebisch, E.F. Healy, J.J.P. Stewart, M. Frazer, D.M. Hayes, HyperChem Computational Chemistry Software Package, Version 8.0, Hypercube, Inc., Gainsville, FL, 2004.
[36] M.J. Frisch, G.W. Trucks, H.B. Schlegel, G.E. Scuseria, M.A. Robb, J.R. Cheeseman, G. Scalmani, V. Barone, B. Mennucci, G.A. Petersson, H. Nakatsuji, M. Caricato, X. Li, H.P. Hratchian, A.F. Izmaylov, J. Bloino, G. Zheng, J.L. Sonnenberg, M. Hada, M. Ehara, K. Toyota, R. Fukuda, J. Hasegawa, M. Ishida, T. Nakajima, Y. Honda, O. Kitao, H. Nakai, T. Vreven, J.A. Montgomery Jr., J.E. Peralta, F. Ogliaro, M.J. Bearpark, J. Heyd, E.N. Brothers, K.N. Kudin, V.N. Staroverov, R. Kobayashi, J. Normand, K. Raghavachari, A.P. Rendell, J.C. Burant, S.S. Iyengar, J. Tomasi, M. Cossi, N. Rega, N.J. Millam, M. Klene, J.E. Knox, J.B. Cross, V. Bakken, C. Adamo, J. Jaramillo, R. Gomperts, R.E. Stratmann, O. Yazyev, A.J. Austin, R. Cammi, C. Pomelli, J.W. Ochterski, R.L. Martin, K. Morokuma, V.G. Zakrzewski, G.A. Voth, P. Salvador, J.J. Dannenberg, S. Dapprich, A.D. Daniels, Ö. Farkas, J.B. Foresman, J.V. Ortiz, J. Cioslowski, D.J. Fox, Gaussian 09, Gaussian, Inc., Wallingford, CT, USA, 2009.
[37] G. Scalmani, M.J. Frisch, Continuous surface charge polarizable continuum models of solvation. I. General formalism, J. Chem. Phys. 132 (2010).
[38] C. Altona, M. Sundaralingam, Conformational-analysis of sugar ring in nucleosides and nucleotides - new description using concept of pseudorotation, J. Am. Chem. Soc. 94 (1972) 8205–8212.
[39] M. Sundaralingam, Structure and conformation of nucleosides and nucleotides and their analogs as determined by X-ray diffraction, Ann. N. Y. Acad. Sci. 255 (1975) 3–42.
[40] A. Filippi, C. Fraschetti, F. Rondino, S. Piccirillo, V. Steinmetz, L. Guidoni, M. Speranza, Protonated pyrimidine nucleosides probed by IRMPD spectroscopy, Int. J. Mass Spectrom. 354 (2013) 54–61.